Chemical Engineering Journal 499 (2024) 156299

Contents lists available at ScienceDirect

Chemical Engineering Journal

journal homepage: www.elsevier.com/locate/cej

Enhanced selective oxidation of ethylarenes using iron single atom catalysts embedded in Nitrogen-Rich graphene

Biagio Di Vizio [a], Dario Mosconi [a], Matías Blanco [a,*], Panjuang Tang [a], Luca Nodari [a,b], Ondřej Tomanec [c], Michal Otyepka [c,d], Simone Pollastri [e,f], Stefano Livraghi [g], Mario Chiesa [g], Gaetano Granozzi [a], Stefano Agnoli [a,h,**]

[a] Department of Chemical Sciences and INSTM Unit, University of Padova, Via F. Marzolo 1, 35131, Padova, Italy
[b] Istituto di Chimica della Materia Condensata e di Tecnologie per l'Energia, ICMATE-CNR, 35127 Padova, Italy
[c] Regional Centre for Advanced Technologies and Materials, Czech Advanced Technology and Research Institute (CATRIN), Palacký University Olomouc, Šlechtitelů 27, 783 71 Olomouc, Czech Republic
[d] IT4Innovations, VŠB-Technical University of Ostrava, 17 Listopadu 2172/15, Ostrava, Poruba 708 00, Czech Republic
[e] Elettra-Sincrotrone Trieste, Area Science Park, Basovizza, Trieste, Italy
[f] Department of Physics, Computer Science and Mathematics, University of Modena and Reggio Emilia, Via Campi 103, 41125 Modena, Italy
[g] Department of Chemistry, University of Torino and NIS, Via P. Giuria 9, 10124 Torino, Italy
[h] Consorzio Interuniversitario Reattività Chimica e Catalisi-CIRCC, Research Unit at the University of Padova, Via F. Marzolo 1, 35131 Padova, Italy

ARTICLE INFO

Keywords:
Race
Maternal Health
Perinatal
Pregnancy
Sleep
Immune Function
Cardiovascular Health
Heart Rate Variability
Preterm Birth
Structural Racism
Health Inequity

ABSTRACT

Heavily (19 % wt) Nitrogen doped graphene (N-G), with Nitrogen incorporated mainly as pyridinic species (77.8 %), was obtained by reacting fluorographene with ammonia under solvothermal conditions, at mild temperature (140 °C). N-G was used to stabilize single iron atoms (N-G-Fe) in two different configurations: low spin X-($Fe^{II}N_4$)-Y and high spin X-($Fe^{III}N_4$)-Y. The resulting N-G-Fe single atom catalysts exhibit remarkable efficacy in the selective oxidation of ethylarenes, with activity comparable or even superior to state-of-the-art materials, converting ethylbenzene to acetophenone with an initial turnover frequency of 13400 h^{-1}. Notably, N-G-Fe exhibits genuine catalytic activity since it is able to oxidize ethylbenzene using substoichiometric amount of peroxides, and exploiting molecular oxygen as the final oxidant. Moreover, N-G-Fe can be recycled without any metal leaching, and exhibits a broad catalytic scope. Multi-technique characterizations combined with rationally designed catalytic tests allowed us to identify the active sites and propose a plausible mechanism for the catalytic cycle.

1. Introduction

Nowadays, over 90 % of the chemical reactions involve the utilization of a catalyst [1], nonetheless many industrial processes are still energy inefficient and with limited selectivity, or the catalytic materials are expensive with a difficult supply. Therefore, the development of highly active catalysts is crucial to realize sustainable and cost-effective chemical processes. The two principal categories of catalysts, homogeneous and heterogeneous, have complementary advantages and drawbacks [2,3], and over the past few decades, the quest for hybrid solutions that combine their benefits has been very intense and challenging [4,5]. One of the most popular strategies consists in the integration of single metal (SA) centres within a precise environment onto an insoluble support [6]. This approach, aimed at achieving the utmost limit of single atoms, ensures optimal atom economy [7] and often enhances activity and selectivity by leveraging the new properties that emerge at the SA regime [8–12]. The primary obstacle in synthesizing SA catalysts (SACs) lies in achieving a high atom density while simultaneously averting aggregation. A large body of literature indicates that graphene (G) based materials are suitable for SA formation and stabilization.

Several efforts have been taken to produce a large library of doped G materials [13–16]. The most used heteroatom is nitrogen (N-doped-G, hereafter N-G), which also changes the electronic properties of pristine G due to the injection of extra electrons in the conduction band [17,18].

* Corresponding author.
** Corresponding author at: Department of Chemical Sciences and INSTM Unit, University of Padova, Via F. Marzolo 1, 35131 Padova, Italy.
E-mail addresses: matias.blanco@uam.es (M. Blanco), stefano.agnoli@unipd.it (S. Agnoli).

https://doi.org/10.1016/j.cej.2024.156299
Received 1 June 2024; Received in revised form 21 August 2024; Accepted 29 September 2024
Available online 5 October 2024

According to previous reports, N can be found in the form of pyrrolic, pyridinic, or graphitic species [19,20]. Typical N-G synthesis methods require annealing temperatures higher than 700 °C [21], which are necessary to reconstruct the carbon scaffold and promote a substantial incorporation of nitrogen in the aromatic structure. Unfortunately, these harsh conditions represent a significant technological shortcoming that decreases the efficiency of the synthesis and hinders the implementation of N-G in large-scale applications. Lower temperature syntheses have been attempted, but using dangerous or toxic reagents such as tetrachloromethane and lithium nitride [22].

Recently, a new synthetic approach that merges synthesis and post-functionalization has been proposed based on the fluorographene (F-G) chemistry [23]. F-G can be described as a perfluorinated hydrocarbon that is able to react as an electrophile under mild conditions. Several examples have been reported where F-G reacts with bases to form prototypical graphene oxide structures [24], with Grignard reagents to yield functionalized G [25], classic nucleophiles as CN– or diethyl malonate to produce G derivatives with a highly functionalized basal plane [26–28], or with organometallic compounds to produce hybrid structures on the material surface [29]. Indeed, theoretical calculations demonstrated that the C-F bond in F-G is labile and prone to react with nucleophilic species [30]. The incorporation of nitrogen into graphene lattice via F-G chemistry was also demonstrated recently [31–34].

Herein, we report on the solvothermal synthesis of highly doped N-G (up to 19 % of N) taking advantage of the F-G chemistry, exploiting the nucleophilic addition and further carbon network integration of NH3 at very mild temperature (140 °C). While the residual fluorine content is minimal after the synthesis reaction, the yielded N-G material demonstrates up to 77 % selectivity towards pyridinic nitrogen, marking the highest observed among N-G derived from F-G. The presence of pyridine sites is crucial for obtaining suitable sites to create effective single-atom catalysts [35]. Selectively obtaining a large quantity of these sites by controlled, low-temperature synthesis without hazardous reagents means a major advance for the development of the field.

N-G is widely used as catalyst in different and important reactions, especially in oxidations, which represent 30 % of the global chemical production. In particular, the oxidative activation of C–H bonds is one of the most employed reactions in the (petro)chemical and pharmaceutical industries, which typically targets the production of added value molecules and commodities [36]. For instance, the selective activation of methylene C-H bonds poses a considerable challenge due to their common presence in organic compounds and their inertness towards most reagents [37,38]. In this paper, we prepare and characterize atomically dispersed Fe atoms (Fe-SACs) immobilized on N-G (N-G-Fe) through a simple impregnation procedure that allows obtaining N-G-Fe hybrid materials with different metal concentrations. The resulting N-G-Fe materials demonstrate an excellent catalytic activity in the hydroperoxide-mediated selective oxidation of alkylarenes. Remarkably, we demonstrate that molecular oxygen serves as the ultimate oxidant and also established the feasibility of employing sub-stoichiometric amounts of peroxide, thereby confirming the genuinely catalytic nature of this oxidation reaction. Remarkably, in this specific chemical conversion, the presence of Fe-SACs imparts greater activity, stability, and selectivity compared to supported FeO_x nanoparticles (NPs) obtained at higher concentrations of the metal precursor. Furthermore, our most active catalyst exhibits a broad scope and an exceptional recyclability. Trough a combination of various spectroscopic investigation and analysis of experiments testing different reaction parameters, we could formulate hypotheses regarding the catalytic sites and the reaction mechanism.

2. Materials and methods

All chemicals were purchased from Aldrich. Reagent grade or better quality was employed in all experiments. All air-sensitive reactions were carried out under N2 atmosphere employing Schlenk lines and N2 degassed solvents. During this study we used N-doped reduced graphene oxide (N-rGO) as a benchmark. For its preparation, graphene oxide (GO) was synthetized according to a modified Hummers procedure [39], and then, N-rGO was obtained by thermal annealing at 900 °C (1 h under Ar) employing 1 g of 1:5 mixture of GO and melamine [40].

2.1. N-G hydrothermal synthesis

If not otherwise stated, in a typical synthesis of N-G (see Scheme 1), an amount of 120 mg (4 mmol) of fluorographite was suspended in 13 mL of N_2 degassed *N*-methyl pyrrolidone (NMP) in a Schlenk-type flask. The suspension was sonicated for 4 h at room temperature (rt) under inert atmosphere. After that, the flask was cooled to 0 °C with an ice bath, and then dry NH_3 was bubbled for 2 h. The NH_3 flux was generated by heating at 60 °C 200 mL of a 28 % NH_3 water solution under stirring; the resulting vapors were dried through a KOH glass frit. Afterwards, the NH_3-saturated NMP solution containing exfoliated F-G was immediately transferred into a 23 mL polytetrafluoroethylene (PTFE) reaction vessel, closed and introduced in an autoclave. To minimize a possible NH_3 loss, the whole autoclave system was previously cooled down below 4 °C. The autoclave was then allowed to naturally reach rt, and then was heated to 140 °C for 60 h (ramp of 1 °C/min) in an electric oven. When the reaction was completed, the autoclave was allowed to cool down to rt, and the black powder was profusely washed by filtration through a PTFE membrane (0.2 μm pore size). Byproducts, mainly white salts (see Figure S1 in the Supporting Information, S.I.), were eliminated by extensive rinsing with different solvents (*i.e.* 3 x 50 mL of *N*,*N*-dimethylformamide (DMF), 3 x 50 mL of water, 3 x 50 mL of 2-propanol and 3 x 50 mL of acetone). Furthermore, after each filtration cycle, the solid cake was collected from the filter, suspended in fresh solvent and sonicated for 5 min to assure that no impurity remained physisorbed. Finally, the resulting N-G was dried in vacuum. Similar results were obtained starting from 240 mg (8 mmol) or 480 mg (16 mmol) of F-G.

2.2. Physicochemical characterization of materials under study

The surface chemical characterization of the materials has been carried out using X-ray photoemission spectroscopy (XPS) in a custom-made UHV system working at a base pressure of 10^{-10} mbar, equipped with an Omicron EA125 electron analyzer and an Omicron DAR 400 X-ray source with a dual Al–Mg anode. Core level photoemission spectra (C 1s, N 1s, O 1s, F 1s and Fe 2p) were collected at rt with a non-monochromatic Mg K_α X-ray source (1253.6 eV) and using an energy step of 0.1 eV, 0.5 s of integration time, and 20 eV of pass energy. The samples were suspended in 2-propanol and drop casted on an Au-coated Al metal support. Samples were measured by High Resolution Transmission Electron Microscope (HRTEM) Titan G2 60–300 (FEI) with Image corrector on accelerating voltage of 80 kV. Images were taken with BM UltraScan CCD camera (Gatan). Energy Dispersive Spectrometry (EDS) was performed in Scanning TEM (STEM) mode by Super-X system with four silicon drift detectors (Bruker). STEM images were taken with HAADF detector 3000 (Fishione). Scanning Electron Microscopy (SEM) images were acquired using a field emission source equipped with a GEMINI column (Zeiss Supra VP35) and micrographs were obtained with an acceleration voltage of 5 or 10 kV using the in-lens high-resolution detector. The Raman spectra were collected using a ThermoFisher DXR Raman microscope using a laser source with an

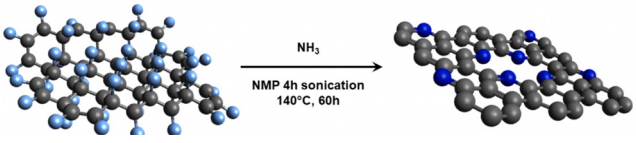

Scheme.1. Synthesis of N-G material. Carbon atoms in grey, fluorine atoms in cyan and nitrogen atoms in blue.

excitation wavelength of 532 nm (1 mW), focused on the sample with a 50x objective (Olympus). The UV−visible absorption spectroscopy data were acquired using a Cary 50 spectrometer (Varian), in the 200–800 nm range. In this case, powder samples were dispersed in DMF, forming a stable colloidal dispersion. Solid state Fourier Transformed Infrared (FT-IR, KBr disk technique) absorption spectra were recorded with a Nicolet Nexus FT-IR spectrometer. Inductive coupled plasma spectroscopy (ICP) measurements were performed in an Agilent Technologies 7700X ICP-MS, equipped with an octupolar collision cell operating in kinetic energy discrimination mode for the removal of polyatomic and argon-based interferences. ζ-potential measurements were carried on Malvern Panalytical Zetasizer Nano ZS90 using 0.1 mg mL^{-1} suspensions of N-G in water. The pH was tuned between 3 and 11 using NaOH and HCl. X-ray diffraction (XRD) data were recorded on a Panalytical Aeris Research instrumentation, using Cu K_α radiation ($\lambda = 0.15406$ nm) at 30 kV and 15 mA. Nuclear Magnetic Resonance (NMR) spectra were recorded on a Bruker Avance 300 MHz (300.1 MHz for ^1H, 298 K); chemical shifts (δ) are reported in units of parts per million (ppm) relative to the residual solvent signals and coupling constants (J) are expressed in Hz. ^{57}Fe Mössbauer spectroscopy was performed at rt on a conventional constant acceleration spectrometer mounting a Rh matrix ^{57}Co source, nominal strength 1850 MBq. The spectra were fitted to Lorentzian line shapes with the minimum number of components by using Recoil software. Hyperfine parameters were obtained by means of standard least-squares minimization techniques; isomer shift (δ), quadrupole splitting (Δ), half linewidth at half maximum (Γ_+), were expressed in mms^{-1}, the relative area (A) in %. δ is quoted relative to α-Fe foil. Fe K-edge XAS spectra were collected at the XAFS beamline (ELETTRA, Trieste, Italy) [41], during experiment 20205038, in transmission mode using a fixed exit double crystal Si (111) monochromator. Energy calibration was accomplished by collecting simultaneously a reference spectrum of Fe metal foil placed in a second experimental chamber after the sample and after the I1 ionization chamber, with the position of the first inflection point taken at 7112.0 eV. The XANES spectra of samples and model compounds were normalized with respect to the atomic background of the curve using the Athena software [42]. EXAFS refinement was also performed, extracting the signal using Athena, Fourier transforming with an Hanning window in the k range 2.15–11.7 $Å^{-1}$ and quantitative analysis were carried out using the Artemis software (Demeter 0.9.25 package). Solid state Continuous Wave Electron Paramagnetic Resonance (CW-EPR) measurements were performed with a Bruker EMX spectrometer operating at X-band (9.5 GHz), equipped with a cylindrical cavity operating at 100 kHz field modulation. The samples were investigated in vacuum after outgassing at rt (residual pressure $P < 10^{-4}$ mbar) at the liquid nitrogen temperature (77 K). The radical species in solution were monitored via spin trapping experiments using an ADANI SPINSCAN X EPR spectrometer associated with the spin trapping agent DMPO (5,5-dimethyl-1-pyrroline-*N*-oxide). In a typical experiment 0.107 g (1 mmol) of ethylbenzene was suspended with magnetically stirring in 4 mL of H_2O. To this mixture, 1 mL of spin trap solution (DMPO 0.088 M), 0.276 g (3 mmol) of *tert*-butyl hydroperoxide and 1 mg of catalyst (N-G-Fe_{dil}) were added, and the reaction was maintained at 65 °C and the EPR spectra were recorded on a sample suspension (50 μL) withdrawn at the desired time. Higher temperature was not employed due to the instability of the DMPO.

2.3. Preparation of the N-G-Fe and N-rGO-Fe hybrid materials

After the synthesis, N-G and N-rGO were impregnated with soluble iron salts to yield N-G-Fe and N-rGO-Fe. Typically, an amount of 30 mg of N-doped G (N-G or N-rGO) was suspended in 30 mL of DMF and sonicated for 5 min. Then, $FeSO_4$ heptahydrate was added in two concentrations: 40-fold diluted vs the amount of N determined by XPS (2.8 mg for N-G and 0.4 mg for N-rGO) and 4-fold diluted vs the amount of N (27.8 mg for N-G and 4.1 mg for N-rGO). The reaction was maintained at 100 °C under magnetic stirring for 16 h. Then, the sample was allowed to cool down naturally to rt, and the resulting black powder was separated by filtration through a PTFE membrane (0.2 μm). The washing procedure was performed employing 3x50 mL of fresh DMF, 2x50 mL of HCl aqueous solution (pH = 3), water until neutral pH, and 2x50 mL of acetone. Vacuum drying yielded the final samples named as N-G-Fe_{dil}, N-G-Fe_{conc} and N-rGO-Fe_{dil}. The Fe titration experiments were carried out using a N-G concentration of 3 mg mL^{-1} and examining concentrations of the metal precursor from 10 mM to 0.1 mM. The impregnation procedure was performed as above, but in this case, the solid was separated by centrifugation and the remaining supernatant was analyzed by UV–VIS spectroscopy.

2.4. Catalytic tests

If not otherwise stated, the catalytic ethylbenzene (EB) oxidation was performed, in a 20 mL open air glass reactor where an amount of 0.107 g (1 mmol) of EB was suspended by magnetic stirring in 5 mL of water. To this mixture, 0.276 g (3 mmol) of *tert*-butyl hydroperoxide (TBHP) and 1 mg of N-G-Fe catalyst were added, and the reaction was maintained at 100 °C for the desired time, typically 1 h. After this, the reactor was allowed to cool down to rt, the crude was diluted with more water, and extracted 3 times with dichloromethane (DCM). The collected organic fraction was dried and concentrated under reduced pressure to submit the crude to NMR analysis (data reported in the Supporting Information file.). On the other hand, the catalyst was recovered by filtration through a PTFE membrane (0.2 μm), washed with acetone/water mixture, dried and re-used for a new catalytic cycle. This procedure was repeated 5 times. The scope of the catalyst was performed in the same way using 1 mmol of the corresponding modified ethylarene substrate. Reactions with control catalysts (N-rGO, N-rGO-Fe, N-G and molecular counterparts) were performed in the same conditions for 16 h. To calculate turnover number (TON) and initial turn over frequency (TOF) TOF_0, we assumed that single atoms of iron were the catalytic centers, whose amount was determined based on the ICP-MS measurements.

The equation used for quantifying the TON is: $TON = \frac{n_{product}}{n_{Fe}}$, where n is the number of moles. The equation used for TOF_0 is: $TOF_0 = \frac{TON}{time}$.

3. Results ad discussion

3.1. Physicochemical characterization of the N-G and N-G-Fe materials

The synthesis of highly doped N-G was performed through the solvothermal reaction of NH_3 with NMP-exfoliated F-G, following a protocol (described in the experimental section) that can be easily scaled up to the gram scale. No F 1s is detected in the XPS spectra, (Figure S2 and Table S1 in the S.I.), and the binding energy (BE) position of the C 1s peak shifts from 291.0 eV, typical of C-F bonds [24], to 284.4 eV (Fig. 1a). These data clearly indicate that defluorination has occurred, leading to the formation of C sp^2 domains. [23]. Moreover, FTIR and Raman spectra (Figure S3 at S.I.) are consistent with the XPS analysis: the typical sharp C-F vibrational band (~1200 cm^{-1}) vanishes, whereas new bands related to C-N (~1160 cm^{-1}) and C=C (~1550 cm^{-1}) vibrations emerge [26]. In addition, while F-G vibrational modes are Raman silent, the N-G Raman spectrum exhibits the typical D (at 1341 cm^{-1}) and G bands (at 1590 cm^{-1}) of G materials [43] (see inset in Figure S3). X-ray diffractograms support the formation of a sp^2 network, since after synthesis, the (002) reflections typical of G materials produce a sharp signal at 26° (Figure S4 at S.I.) [33], producing a very different pattern compared to the parent F-G. Regarding the nitrogen content of the N-G material, an intense N 1s core level peak is detected in the XPS survey (Figure S2 at S.I.). Interestingly, the elemental analysis of the sample carried out both by combustion analysis and XPS (Table S1) provides an almost similar N content (19 at. % by XPS and 17.6 at. % by combustion), in any case among the highest loading reported in the

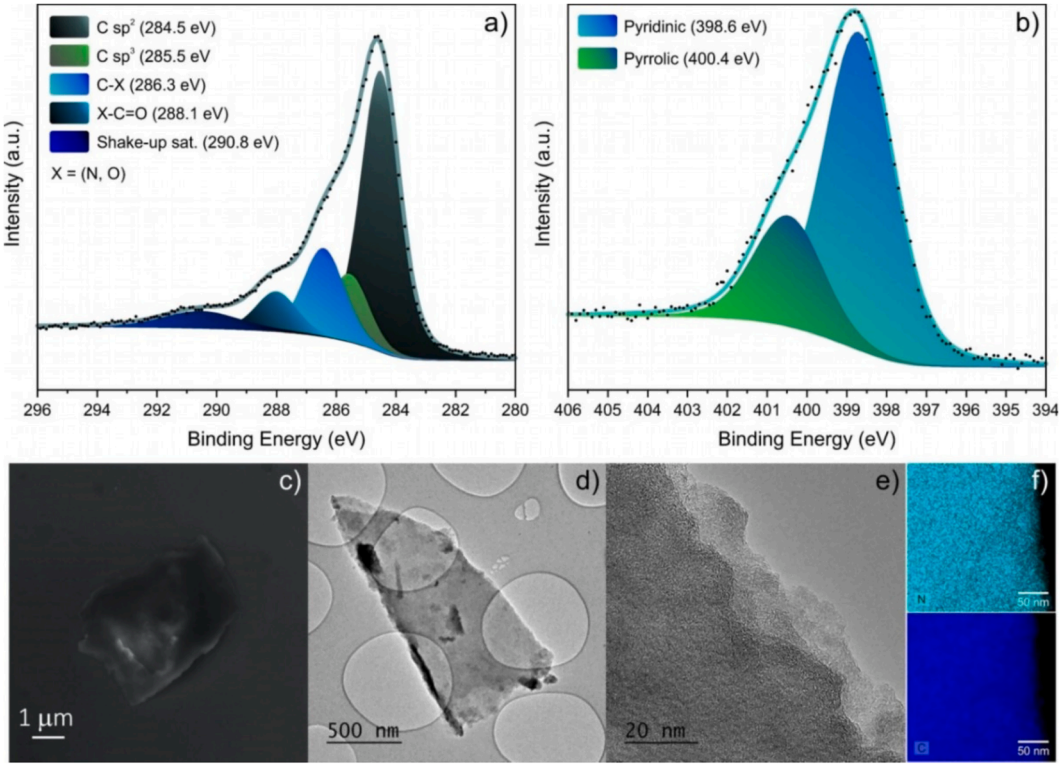

Fig. 1. A) c 1s and b) N 1s XPS core level region of sample N-G. Morphological analysis by c) SEM, d) and e) HRTEM and f) EDX elemental mapping (cyan: N; blue; C). (For interpretation of the references to colour in this figure legend, the reader is referred to the web version of this article.)

literature [31,32,44,45]. Deconvolution of the N 1s photoemission peak reveals two main components at 398.6 eV and 400.4 eV, which can be assigned to pyridinic and pyrrolic nitrogen species, respectively (Fig. 1b) [18–20], where the former represents approximately 80 % of the total signal. Amine related signals were absent in the FTIR spectra of the sample and a standard Kaiser test for the presence of primary amine was negative, in agreement with the XPS analysis. In addition, the oxygen content was very low, in the 5 at. % range as determined by XPS. The N-G morphology was investigated by SEM and HR-TEM (Fig. 1c-e): the typical flake-like structure of exfoliated few layer/monolayer G, with sheet lateral sizes in the range of 500–1000 nm is observed, in agreement with previous results of G derivatives obtained starting from fluorographite [4,26,46,47]. Moreover, nitrogen is homogeneously distributed on both the basal plane and edges of the individual sheets (see EDX elemental map in Fig. 1f). The ζ-potential curve of N-G as a function of pH is reported in Figure S5 at S.I., where at acidic pH the neat charge of the material is positive as a consequence of the protonation of the N atoms. Conversely, at pH values between 4 and 10, the material bears a neat zero charge, and negative charge above pH 10, possibly due to adsorption of ions on the surface of the material or a deprotonation of pyrrolic sites. The high density of coordinating nitrogen groups makes N-G a perfect platform for supporting highly dispersed metal species. We impregnated the N-G with iron cations (one of the most earth abundant and non-toxic metals useful as a catalyst in several reactions) [48] using $FeSO_4$ as a precursor. Firstly, we determined the saturation concentration of iron in the N-G sample through a titration procedure, using $FeSO_4$ solutions in DMF ranging from 0.1 mM to 5.0 mM. The impregnation was performed for 16 h at 100 °C, then the resulting suspension was centrifuged and the supernatants were analyzed by UV–Vis spectroscopy, looking carefully at the optical fingerprints of remaining $FeSO_4$ (Fig. 2a) [48]. Interestingly, the metal precursor peaks in the 300–350 nm region became visible only at a concentration higher than 2.25 mM, while below this limit, the $FeSO_4$ signal was absent. Therefore, this titration suggests that if the concentration of the precursor is kept below the saturation limit, all the added iron cations are sequestrated from the solution and coordinated to N-G. With these data in mind, we investigated two N-G-Fe samples at different metal loading, as described in Fig. 2b. The initial sample, named N-G-Fe_{dil}, was produced using a $FeSO_4$ concentration of 0.34 mM in DMF, which is significantly below the saturation limit. HAADF STEM and HRTEM/EDX analysis (Fig. 2e, figure S7a) demonstrates that Fe-SACs are homogeneously distributed on the N-G surface and only very low amounts of NPs can be found after extensive observations. The Fe loading detected by ICP was about 1 % wt. (see Table S3 in the S.I.). In addition, the Fe 2p photoemission spectrum of N-G-Fe_{dil} is indicative of Fe-N bonds, where iron is present either as Fe(II) or Fe(III) (Figure S11) [49,50], whereas no presence of SO_4^{2-} could be observed by XPS. Moreover, upon examining the N 1s photoemission line, a new peak has to be included to achieve a satisfying fitting (Fig. 2c). This peak (centered at a BE of 399.7 eV) amounts 20 % of the signal, and it is usually associated with N-Fe bonds [51]. Therefore, the whole set of XPS data suggests that during the impregnation procedure, the starting Fe(II) precursor is partially oxidized to Fe(III) and iron cations are coordinated as SACs to the nitrogen species of N-G nanosheets. In order to have a benchmark, a prototypical N-rGO, synthetized by treating GO obtained by Hummers' synthesis with melamine at 900 °C, was impregnated with Fe precursors at the same concentration used above. In this case, the amount of Fe bonded to N is lower (0.15 %wt. according to ICP determinations, Table S3 at S.I.). Therefore, our N-G is more effective at coordinating Fe ions compared to the standard N-rGO surface, with a ratio of 0.0125 Fe atoms per atom of nitrogen vs 0.00625 Fe/N in N-rGO. This difference is likely associated with the higher level of N doping that makes statistically more probable the presence of N_4 macrocycles that are known to be extremely effective for metal coordination. We investigated also a N-G-Fe sample with a higher iron loading (N-G-Fe_{conc}) obtained by impregnating N-G in DMF under the same experimental conditions of the previous hybrid material, but using a 3.4 mM $FeSO_4$ solution, *i.e.*, a concentration of the metal precursor significantly higher than the saturation limit. HRTEM/EDX

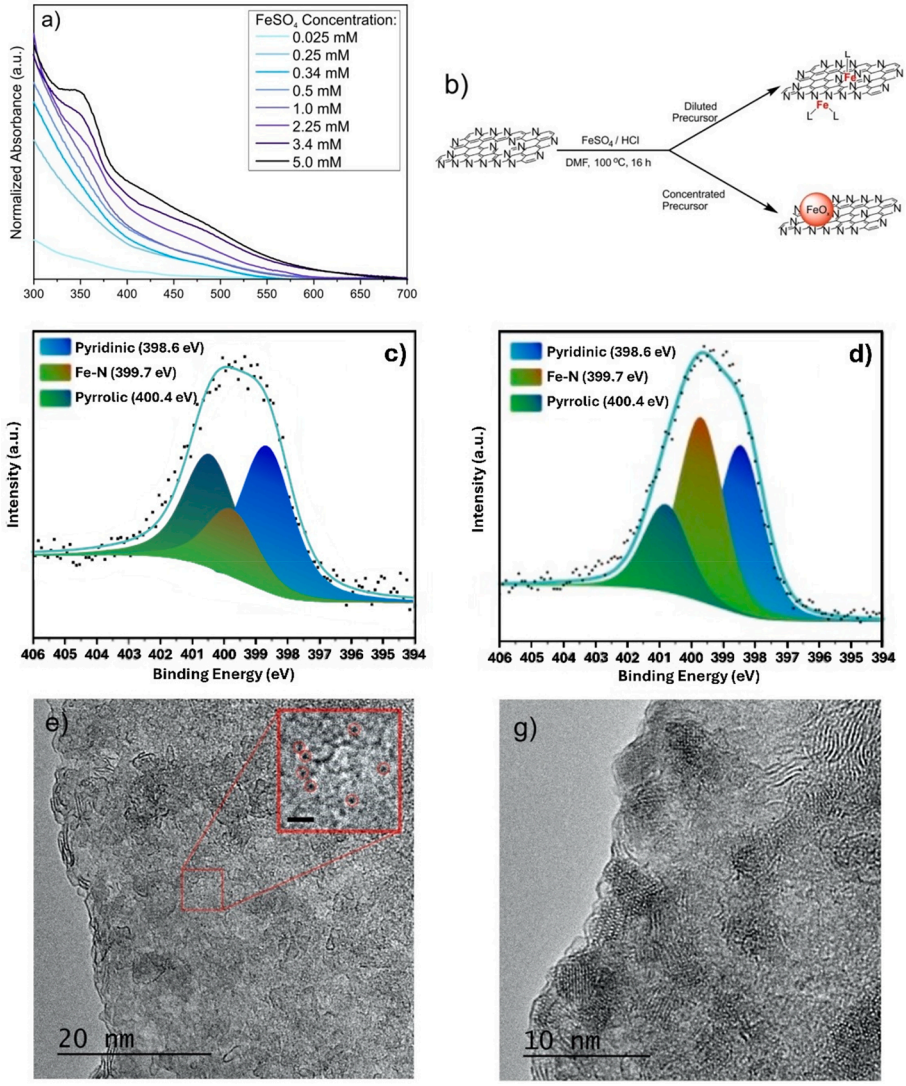

Fig. 2. Characterization of the N-G-Fe samples. a) titration procedure carried out through UV–VIS spectra of the supernatant solutions after the impregnation of N-G with $FeSO_4$ at different concentration, b) Scheme of Fe impregnation, c) and d) N 1s XPS core level region of N-G-Fe_{dil} and N-G-Fe_{conc} respectively, e) HAADF STEM image of N-G-Fe_{dil} (inset: digital zoom, scale bar 1 nm) with and f) HAADF STEM image of N-G-Fe_{conc}.

data revealed NPs with a mean size of 3.1 nm (Figure S8 in the S.I.), which are mainly located at the edges of the sheets, as shown in Figure S10. The EDX elemental maps indicated that such NPs are mainly composed of iron oxides due to the systematic spatial correlation between the O and the Fe signals (Figure S7 b.). The presence of iron oxide NPs leads to a rather different shape of the Fe 2p photoemission line (Figure S11 in the S.I.). The loading of iron in N-G-Fe_{conc} reaches a remarkable value of 11 wt% as determined by ICP (Table S3 at S.I.). In addition, the N 1s XPS core level region (Fig. 2d) presents the same components discussed in the most diluted sample, but in this case, the intensity of the peak corresponding to Fe-N bonds accounts 45 % of the total signal. Interestingly, in both Fe-loaded samples, this component reaches similar values of the total N 1s core level region, indicating a saturation behavior of pyridinic/pyrrolic moieties above a certain amount of iron atoms, in agreement with the Fe titration experiments. The optical absorption spectrum of N-G-Fe_{conc} suspended in DMF shows an absorption peak at 365 nm, characteristic of Fe NPs,[52] which conversely is absent in the N-G-Fe_{dil} sample.

A more accurate characterization of the local environment and coordination geometry of iron for both N-G-Fe_{dil} and N-G-Fe_{conc} hybrid materials was determined by Mössbauer spectroscopy [53]. The N-G-Fe_{dil} spectrum (Fig. 3a) shows a broad, slightly asymmetric doublet centered around 0.38 mm s^{-1}, suggesting the presence of Fe(II)/Fe(III) sites, in agreement with the XPS measurements. Considering the asymmetry of the doublet, the best fit was obtained using two different sites, Db1 and Db2, whose parameters are reported in Table 1. Interestingly, the hyperfine parameters discard the presence of NPs in N-G-Fe_{dil}, in excellent agreement with the SA distribution extracted from the HRTEM analysis. Db1 shows an isomer shift (δ) that can be tentatively assigned to high spin (HS) $Fe^{III}N_4$ centers with two axial ligands. The relatively low value of quadrupole splitting (Δ) points to a small electric field gradient at the Fe nuclei, highlighting a low distortion of the ferric sites. Similar values of hyperfine parameters were obtained by Liu *et al.* [54]. The authors suggested the presence of X-($Fe^{III}N_4$)-Y sites with the metallic nuclei pulled out of the N-G plane.

It is worth mentioning that Db1 shows a broad line-width (Γ_+ 0.25 mm s^{-1}) that suggests the presence of HS ferric sites with a slightly differing environment. This is probably related to the intrinsic disorder of the G sheet since the synthesis temperature is below 150 °C. A distribution of diverse X-$Fe^{III}N_4$-Y complexes, where X and Y can be assigned to OH, H_2O or even other N atoms present in the graphene scaffold, is indeed expected [54]. On the other hand, a definitive assignment of Db2 is rather difficult to carry out. In fact, it shows a δ value considerably lower than the Db1 one. The presence of another

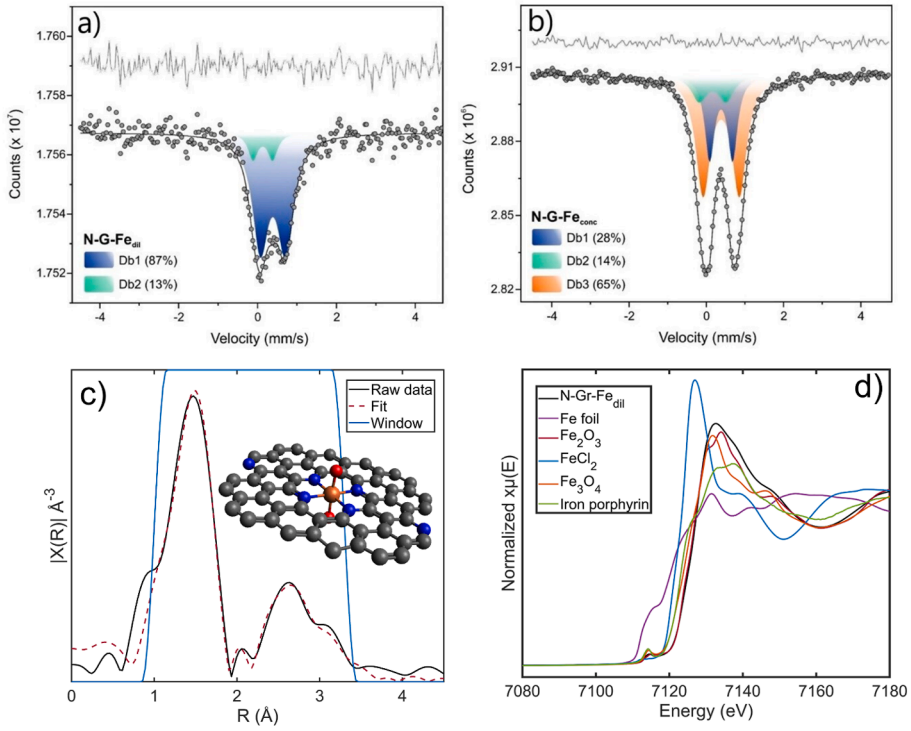

Fig. 3. Room temperature Mössbauer spectra of N-G-Fe$_{dil}$ (a) and N-G-Fe$_{conc}$ (b). (c)N-G-Fe$_{dil}$ EXAFS fit obtained using the structure outlined by the ball and stick model in the background (carbon atoms in gray; nitrogen atoms in blue; oxygen atoms in red and iron atom in orange) d) XANES data of N-G-Fe$_{dil}$ and related standards. (For interpretation of the references to colour in this figure legend, the reader is referred to the web version of this article.)

Table 1
Hyperfine Mossbauer parameters of N-G-Fe samples.

Sample	Site	δ (mm s^{-1})	Δ (mm s^{-1})	Γ+ (mm s^{-1})	A(%)	Assignments
N-G-Fe$_{dil}$	Db1	0.39(4)	0.63(3)	0.25(4)	87 (4)	HS Fe(III)
	Db2	0.13(8)	0.50(1)	0.15(1)	13 (1)	LS Fe(II)
N-G-Fe$_{conc}$	Db1	0.38(1)	0.59(5)	0.15(5)	28 (2)	HS Fe(III)
	Db2	0.16(5)	0.69(5)	0.24(9)	14 (1)	LS Fe(II)
	Db3	0.39(7)	0.94(9)	0.23(2)	65 (3)	NanoOx

δ is quoted relative to α-Fe Foil

ferric site can be excluded because Fe(III) usually shows higher δ values for molecular Fe-N complexes, as for instance, phthalocyanines [55]. According to the literature [56], such low value can be ascribed to a decrease in the number of *d* electrons, and two possible configurations can be found: Fe(IV) configuration or Fe(II) in low spin (LS) configuration. The presence of Fe(IV) was observed by Bouwkamp-Wijnoltz *et al.* [57] in a pyrolyzed carbon-supported iron porphyrin catalysts. Some other authors report the formation of a Fe(IV) center in N-bridged diiron phthalocyanine μ-nitrido dimers [58]. Considering the actual characteristics of the sample N-G-Fe$_{dil}$ and bare N-G support, the assignment of Db2 to LS Fe(II) centre is more realistic than highly oxidized Fe species. Following the assignment for Db1, another X-(Fe^{II}N$_4$)-Y configuration can be proposed, with similar distribution regarding X and Y due to the low-temperature solvothermal procedure adopted. Interestingly, the area ratio between the doublets Db1 and Db2 (87:13) is consistent with the XPS analysis discriminating between Fe(II) and Fe(III) species measured on the same sample, although it must be mentioned that the Fe (II)/Fe(III) is dependent on the duration of the sample exposure to air. Conversely, the increased Fe loading of the sample N-G-Fe$_{conc}$ strongly decreases the asymmetry of the Mossbauer spectrum, as shown in Fig. 3b and the spectrum consists of an intense doublet centered near 0.38 mm s^{-1}. The best fitting was obtained by using three different doublets: Db1, Db2 and Db3. While Db1 and Db2 show hyperfine parameters close to those obtained in N-G-Fe$_{dil}$ (in accordance with the XPS data), Db3, characterized by a huge D value, can reasonably be assigned to nano-sized iron oxides in superparamagnetic regime, according with previous literature data and the characterizations performed [59].

To further understand the local arrangement of iron atoms and confirming the existence of isolated iron species, X-ray absorption spectroscopy (XAS) measurements were conducted on N-G-Fe$_{dil}$. Fe foil, Fe_2O_3, Fe_3O_4, $FeCl_2$ and Fe porphyrin were used as standards. The X-ray absorption near edge structure (XANES) spectra confirm the prevalence of 3+ as oxidation state (Fig. 3d). However, as mentioned above, the ratio of Fe(II) to Fe(III) varies depending on exposure to air and the XANES analysis does not allow us to confirm or exclude the presence of a small amount of Fe(II).The Fourier Transformed extended X-ray absorption fine structure (FT-EXAFS) spectra of N-G-Fe$_{dil}$ and of the two oxides taken as reference are very different, confirming the absence of Fe-O-Fe bonds, while the spectral fingerprint observable between 2 and 4 Å is comparable with the Fe porphyrin reference (Figure S12b at S.I.). The phase-uncorrected FT-EXAFS of N-G-Fe$_{dil}$ cannot be fitted neither with second shell Fe-Fe interactions nor with a normal porphyrin structure. The model used in the fitting (Fig. 3c) is shown in S.I. (Figure S12a) and consists of 4 nitrogen atoms and 2 oxygen atoms in an octahedral coordination in the first shell, in agreement with the structural information provided by Mossbauer data.

The bond distances resulting from the fitting procedure are 2 Å for the first shell comprising 4 nitrogen atoms and 2 oxygen atoms, whereas 2.6 Å and 3.4 Å for the second shell, composed of 4 carbon atoms. With a amp value of 1.08 and an R-factor of 0.009 the fitting can be considered very reliable.

3.2. Catalytic properties of the N-G and N-G-Fe materials

Both N-G and its metalated derivatives are usually employed as oxidation catalyst [60]. Thus, we tested the catalytic activity of the N-G based materials in different oxidation reactions. Starting with the metal-free N-G material, we discovered that it can catalyze the selective oxidation of ethylbenzene (EB) to acetophenone (AP) using *tert*-butyl hydroperoxide (TBHP) at a catalyst loading of 1 % by weight relative to the aromatic substrate (Table 2). This reaction has been previously documented and interpreted as a peroxide-mediated oxidation.[61,62] The reaction kinetics (Fig. 4) was obtained by NMR data, tracking the disappearance of the downfield aromatic peaks of the substrate (~7.0 ppm) and the merging of the upshifted peaks of the product (~8.0 ppm): N-G requires 16 h to yield AP almost quantitatively (92 %), in a reaction that is fully selective (98 %) to the target product (no traces of benzaldehyde or benzoic acid were detected by NMR) (Table 2). When N-G-Fe is used, the reaction is dramatically boosted (Fig. 4).

Indeed, an outstanding reaction time of only 75 min was sufficient for 1 % wt. N-G-Fe_{dil} to yield full conversion to AP, as shown by the kinetic profiles: no induction period was observed and the formation of the keto groups started immediately after the thermal equilibration. Such excellent performance has to be associated with Fe-SACs present in N-G-Fe_{dil}, as clearly confirmed by the turnover number (TON) and initial turn over frequency (TOF_0) values reported in Table 2. When comparing the results with N-G-Fe_{conc}, it is evident that the Fe-SACs in N-G-Fe_{dil} achieve an initial TOF_0 that is two orders of magnitude (13400 h^{-1}) higher than that of the aggregated FeO_x NPs that are present on N-G-Fe_{conc} (812 h^{-1}). Noteworthy, as shown in Table 3, the TOF_0 of N-G-Fe_{dil} is comparable or even superior to state-of-the-art catalysts for this reaction, even considering the different reaction conditions. Control experiments carried out with N-rGO-Fe_{dil} did not achieve a high level of activity (Table 2), confirming that the effective active sites for this reaction are associated with Fe-SACs coordinated to nitrogen species (for a comparison see also Figure S13 at S.I.). The scope of this oxidation has been expanded to other substituted ethylarenes (Fig. 4, lower panel).

Similar performances were obtained using 2-ethylnaphthalene as substrate, highlighting the large tolerance of the catalyst to larger substrates; moreover, longer chains do not influence the conversion process. Substituents in the benzene ring are also well-tolerated: while a *p*-methyl substitution at the phenyl ring does not modify the activity, a *p*-OH (*i.e.* deactivating group) and a *p*-Br substituents to the alkyl group afford values of conversion and selectivity not far from those of the EB experiment. Finally, it is worth noting that the catalyst is fully recyclable, obtaining very similar performances after recovering, washing and using it for a new catalytic cycle for, at least, 5 times (Figure S14 at S.I.). Interestingly, no leaching of Fe has been detected by ICP measurements after cycling of the N-G-Fe_{dil} sample (less than 0.02 % wt. loss, Table S3), whereas a 3.8 % wt. Fe loss is shown for the N-G-Fe_{conc}, together with relevant morphological changes. Actually, after the catalytic work, the FeO_x NPs segregate on the nanosheet edges and reach a mean diameter of 40 nm (Figure S10 at S.I.). This demonstrates once more the superior performance and outstanding stability of the Fe-SACs on N-G-Fe_{dil}.

Table 2
Catalytic parameters of the ethylbenzene (EB) oxidation to AP. 1 % w/w of catalyst respect to the substrate.

Sample	Conv (%)[a]	Time (min)	Select (%)[b]	TON[c]	TOF_0 (h^{-1})[d]
No cat	–	75	–	–	–
N-G	92	960	98	–	–
N-G-Fe_{dil}	>99	75	>99	5587	13,407
N-G-Fe_{conc}	71	75	95	508	812
N-rGO	–	75	–	–	–
N-rGO-Fe_{dil}	6	75	96	225	45

a) Determined by ^{1}H NMR, b) To the target AP, determined by ^{1}H NMR, c) Calculated using the Fe concentration deduced by ICP-MS, d) determined after 5 min of reaction.

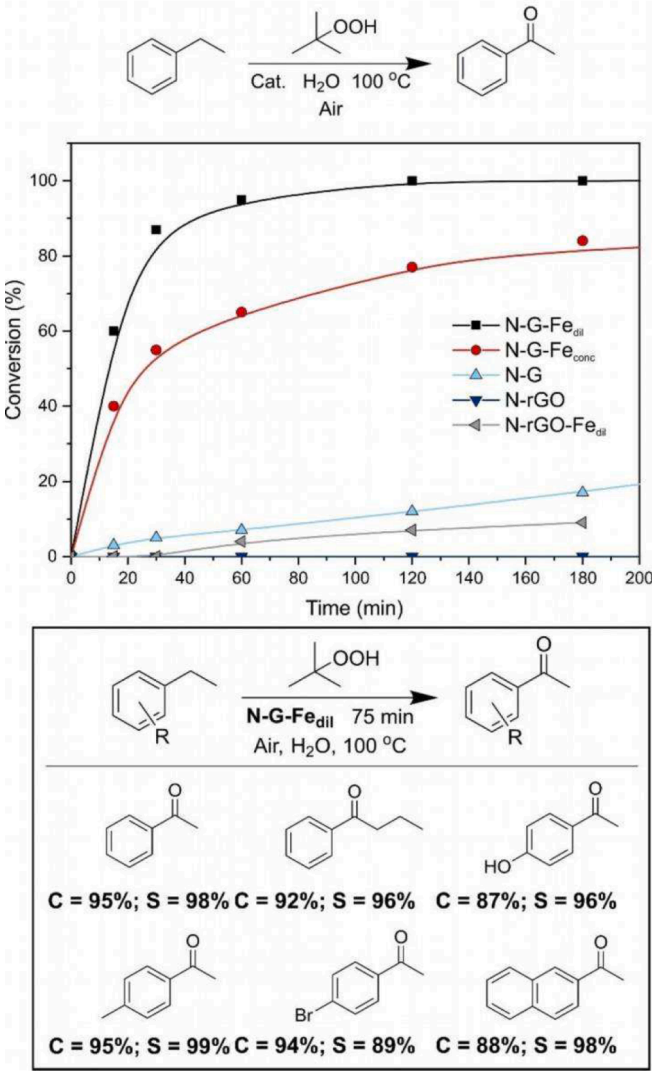

Fig. 4. Upper: time evolution on the oxidation of ethylbenzene (EB) catalyzed by different N-G based materials; lower: summary of Conversion (C) and Selectivity (S) reached using different substrates and the N-G-Fe_{dil} catalyst after 75 min.

To better understand the origin of the catalytic activity, we compared the performance of our graphene-based catalysts with the reactivity of a series of homogeneous catalysts, and we also modified the reaction conditions (solvent, type of peroxide, catalytic substrate, etc.). The results of a wide gamut of experiments are fully reported in the supporting information (Figures S15-S16 and Tables S5-S6 at S.I.), and a brief summary is shown in Table 4. First (Table 4 entry 2), the reaction performed with $FeSO_4$, *i.e.,* the precursor employed in the synthesis of the N-G-Fe catalyst family, afforded full conversion of EB, but with a poor selectivity for AP (Figure S15 at S.I.). Indeed, the reaction is significantly slower and the ratio between the alcohol 1-phenylethanol (PE), a possible reaction intermediate, and ketone is 3/1. Secondly, the role of the Fe sites was analyzed with a kinetic experiment employing molecular iron (III) (tetraphenylporphyrin) chloride (Fe(TPP)Cl). This molecule showed a behavior similar to $FeSO_4$, being able to consume 80 % of EB in the first 5 min of reaction, but an almost equimolar mixture of PE and AP was observed by NMR (Figure S16 at S.I.). Moreover, increasing the reaction time, PE was transformed to AP, in accordance with the literature [54]. However, the performance of the

Table 3
Comparison of the catalytic parameters of the ethylbenzene (EB) oxidation to AP of the present study with respect to selected literature.

Sample	Conv (%)	Time (min)	Solvent	Temperature	Selectivity (%)	TOF (h^{-1})
N-G-Fe_{dil}	>99	75	Water	100 °C	>99	13,407
Co(II)/NHPI [63]	87	600	Acetic Acid	100 °C	97	878.1
Zn-N-C-900 [64]	99	600	neat	80 °C	99	23.7
Mn(II)-Met@MMNPs [65]	47.1	480	Acetic acid	100 °C	98	1287
Fe-MEG-800 [66]	>99	720	Water	25 °C	>99	1006
Co_2Fe-LDH [67]	80	360	Trifluorotoluene	80 °C	91	6.8
$Co_{1.5}Ni_{1.5}Al_1O_x$ [68]	73.7	8 h	Acetic Acid	120 °C	85.1	71.8

Table 4
Changes in the AP selectivity with reaction conditions.

Entry	Variation from standard conditions	AP Select. (%)[a]
1	None	>99
2	Catalyst ($FeSO_4$, FeTPPCl)	20 – 50
3	Peroxide (catalytic TBHP, H_2O_2, $^tBuO-O^tBu$)	98, 11, 43
4	Temperature (70 °C, 90 °C)	25 – 35
5	Solvent (2-propanol, 1,4-dioxane, nonane)	0 – 64
6	Inert atmosphere	8
7	Substrate (PE)	5

[a]Determined by ^{1}H NMR.

heterogeneous N-G-Fe_{dil} catalyst is kinetically different, since PE is detected only in small amounts and catalytic tests starting directly from PE did not produce any AP (Table S6 at S.I.).

A significant point to highlight is that, unlike previous literature where at least two equivalents of peroxide are necessary for full conversion, N-G-Fe_{dil} was able to yield AP employing even a sub-stoichiometric amount of peroxide (3 mol% vs substrate) (Table 4 entry 3 and Table S6 in the S.I.). This key point suggests that the mechanism governing the EB oxidation must be partially different from what was previously suggested in the literature for very similar materials [54,66]. Firstly, starting the reaction directly from the alcohol, only a 5 % conversion was achieved (Table S6 at S.I.), in disagreement with previous works [54]. The formation of PE must be a competitive reaction with the AP formation pathways, and the nature of peroxide, the solvent and the temperature play a fundamental role in the final AP/PE ratio. For instance, the choice of the peroxide is crucial for the selectivity of the reaction (Table 4 entry 3). On the one hand, hydrogen peroxide reverses the selectivity up to 89 % towards PE (Table S6 at S.I.), showing that *tert*-butoxyl radicals own a role in this change. On the other hand, we obtained very low conversion values employing di-*tert*-butyl peroxide due to the higher dissociation energy of the peroxide bond. Indeed, we were never able to reach full selectivity even increasing the reaction time with this particular peroxide (see Table S6 at S.I.). Finally, *tert*-butoxy radical concentration must be higher than that of hydroxyls radicals to guarantee a high selectivity toward AP.

We can draw a similar conclusion observing the trend at lower temperatures from 70 °C to 100 °C (Table 4 entry 4). While the dissociation kinetics of TBHP increases, the selectivity toward AP increases until we obtain full selectivity in the experiment performed at 100 °C. Interestingly, water is the only solvent that leads to complete conversion and full selectivity to AP, while the use of less polar solvents decreases the conversion (Table 4 entry 5), in fact, 92 % conversion is obtained in 2-propanol and 61 % in dioxane, while the selectivity toward AP becomes 8 % and 64 %, respectively (Table S6 at S.I.). Furthermore, conducting the reaction in 1,4-dioxane with TBHP in anhydrous nonane almost completely suppresses the activity. Therefore, water must play a key role in the catalytic cycle. Moreover, performing the reaction under inert conditions (under N_2 atmosphere in degassed solvent) strongly quenches the reactivity (Figure S17 at S.I. and Table 4 entry 6), highlighting the role of molecular oxygen.

Complementary data were provided by *in situ* EPR experiments. As stated in the previous literature, the mechanism follows a radical pathways [54]. Fig. 5 shows the results of the spin-trapping experiments performed on the mixture of reactants in the absence (panel A) and in the presence (panel B) of the N-G-Fe_{dil} Catalyst. Computer simulations enable the assignment of this signal to the simultaneous presence of two paramagnetic species, the hydroxyl radical ($^{\bullet}$OH, black dots in Fig. 5A) which represents the main component, and a weak trace of superoxide ($O_2^{\bullet-}$, triangles in Fig. 5A) species (see Figure S18 at S.I.). A different behavior is observed in the presence of the catalyst. In this case, neither at rt nor at high temperature the previous EPR signals are detected (Fig. 5, panel B). Only a weak signal due to the oxidized form (DMPOX) of the DMPO molecule is detected (stars in Fig. 5B and Figure S18 at S.I.). These data suggest that at 65 °C, the decomposition of the peroxide produces radical species which, however, are not observed in the presence of the catalyst, supporting the idea that they are directly involved in the catalytic process. Finally, at a high catalyst concentration, the spin-trapping experiment clearly reveals the formation of superoxide radical signals (Fig. 5, panel B line c), indicating that this radical species is also generated in the presence of the catalyst.

Considering all the experimental data so far gathered, we can propose the catalytic cycle depicted in Scheme 2. Our experimental evidence and the literature suggest that the metal centers can break homolytically the hydroperoxide bond [69] (step E.1 in the Scheme 2), generating hydroxyls radical OH$^{\bullet}$ and *tert*-butoxyl radicals. These species can easily form EB radicals by hydrogen abstraction, which can either be engaged in a side coupling reaction with a radical hydroxyl group forming PE (T.1) or proceed through the catalytic cycle. On the other hand, it is well known that molecular oxygen is activated by Fe(II), which oxidizes to Fe (III) [70] (S.1). Indeed, *in situ* EPR measurements (Figure S19 at S.I.) confirm that the signal of Fe(III) decreases with time

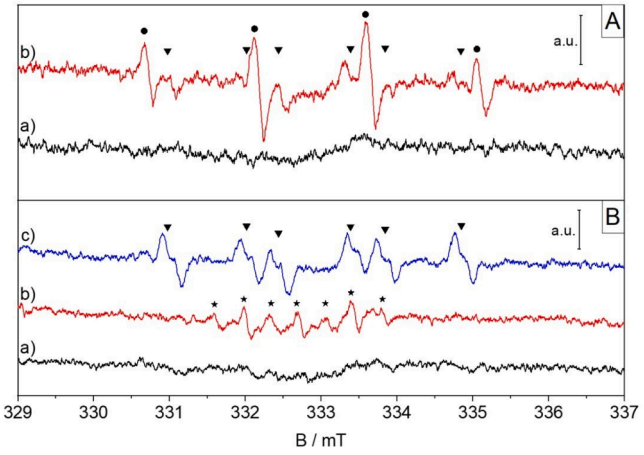

Fig. 5.E. PR spectra obtained with the DMPO spin trapping agent for the mixture of reactants. ● DMPO-OH adduct (dots), ▼DMPO-O_2^- adduct (triangles), x DMPOX (stars). Panel A: without catalyst, a) rt, 30 min of reaction. b) 65 °C, 30 min of reaction. Panel B: with catalyst, a) rt, 30 min of reaction 1 mg of N-G-Fe_{dil}, b) 65 °C, 30 min of reaction 1 mg of N-G-Fe_{dil}, c) 65 °C, 5 min of reaction 2 mg of N-G-Fe_{dil}.

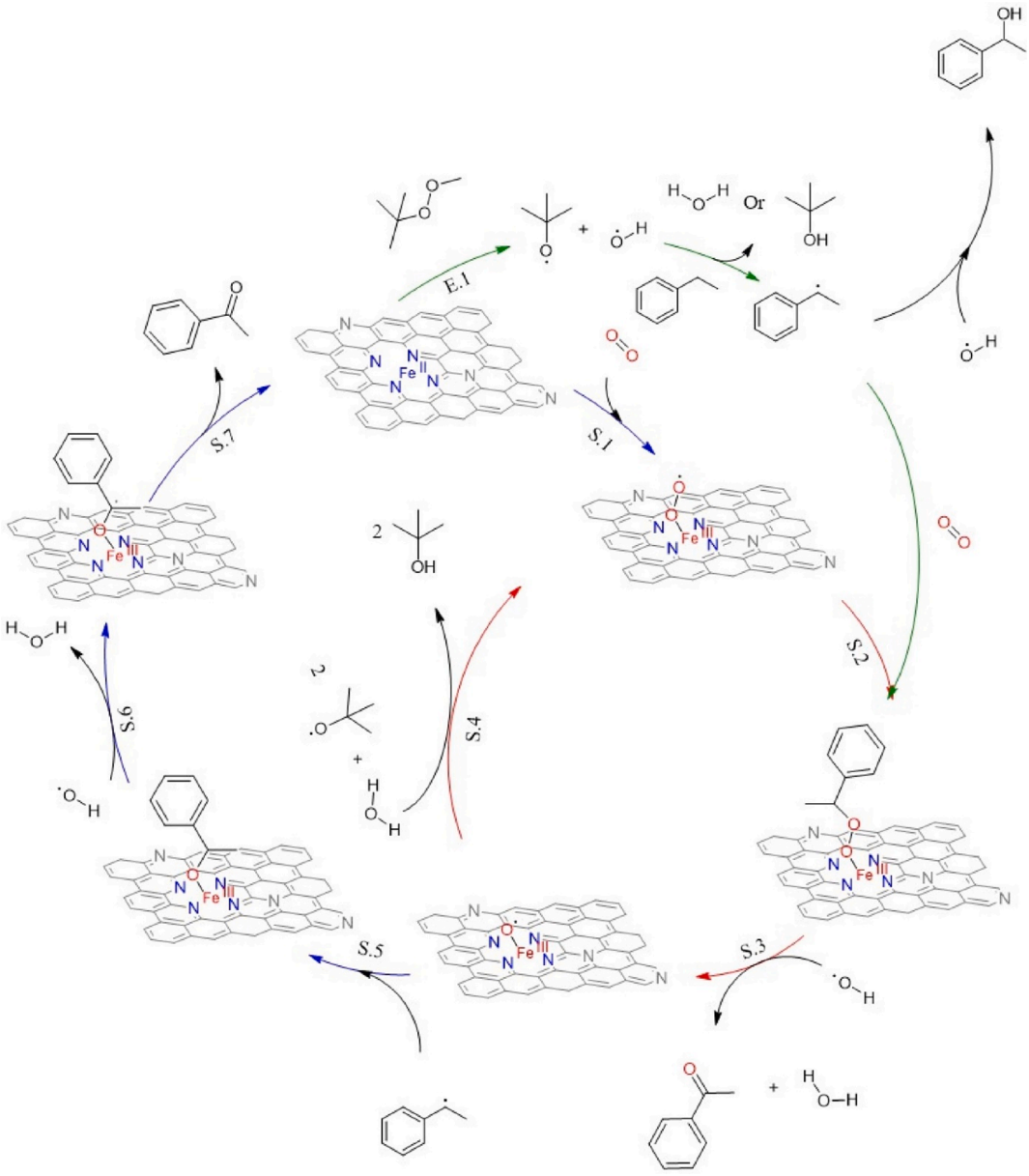

Scheme.2. Proposed reaction mechanism for the EB oxidation.

in anaerobic atmosphere when, as previously mentioned, the reaction stops, explaining the key role of oxygen in the catalytic cycle. The EB radical can react with radical oxygen (S.2) forming a phenylethylperoxo species that, after homolysis of the O-O bond and another hydrogen extraction by hydroxyl or *tert*-butoxyl radicals, can lead to AP (S.3). At this point, the catalytic cycle can be closed through two alternative pathways. In one case, the iron coordinated oxygen radical can be regenerated *via* reaction with water and sequential proton extraction (S.4). The occurrence of this step is justified by our catalytic tests showing that water is needed to reach a full AP yield (Table S6 at S.I.). In the alternative pathway, a new EB radical can react with the radical hydroxyls $OH^{\bullet}$ formed by S.5. A radical can remove a proton (S.6) and then, the α-carbon can be oxidized forming AP, while the iron center is reduced to Fe(II) (S.7), closing the catalytic cycle. To understand the selectivity, we must consider the relative rates of AP and PE formation, which are controlled by the tendency of the EB radical to react with either OH• or the oxygen species activated on the metal centers (S.2 or T.1). Therefore, the local *tert*-butoxyl radical/$OH^{\bullet}$ ratio is a critical parameter for the selectivity, as suggested by the experiments performed with different peroxides (Table 3 and Table S6 at S.I.). When we reduce the concentration of TBHP to a substoichiometric amount (0.03 mmol), a substantial decrease of the selectivity toward AP (72 %), is observed. In this conditions, an heterogeneous Fenton like activity [71] promoted by the iron centers determines a higher concentration of OH• that preferentially react with the EB radical forming PE. Additionally, as shown in S.4, water is crucial for the reaction pathway and the competition between the formation of PE in solution and formation of AP on the material is strictly controlled by the polarity of the reaction medium. A highly polar solvent as water makes more favorable the adsorption of the substrate on the material surface, inhibiting the termination reaction between EB radical and $OH^{\bullet}$ and promoting the heterogeneous pathway. On the other hand, a less polar medium promotes the radical coupling in solution making less probable the heterogeneous pathway. Finally, since the reaction is suppressed in the absence of oxygen and it can proceed in presence of oxygen even with a substoichiometric amount of peroxide, we can conclude that oxygen is the true oxidant and the peroxide is only an activator. To the best of our knowledge, this is the first demonstration that the oxidation of EB can proceed in a genuine catalytic way.

4. Conclusion

In this work, we presented a cheap and energy efficient synthesis protocol to prepare heavily N-doped graphene (19 %) using a low temperature hydrothermal approach that takes advantage of the particular chemistry of F-G. The synthesis temperature can be adjusted to a value as low as 140 °C, ensuring a favorable technological process. This procedure allows reaching record doping levels, much higher than those usually reported in the literature (<∼15 %). It also led to a high selectivity toward the formation of pyridinic-like moieties (close to 80 % of the total N) as evidenced by XPS. This prompted us to impregnate the material with Fe, to generate a N-G-Fe SAC, either in the form of SAs or small NPs as a function of the amount of the Fe precursor. In the SA configuration, the Fe species are coordinated to the N-G structure in two slightly distorted (octahedral) geometries: low spin X-(Fe^{II}N4)-Y, and high spin X-(Fe^{III}N4)-Y. We tested the N-G-Fe SAC toward the oxidation of alkylbenzenes obtaining better catalytic activity compared to pristine N-G and benchmark N-rGO-based control experiments, achieving levels of activity comparable or even superior than the state-of-the-art catalysts. Moreover, despite the lower dosage of metal, the SAC-based catalyst outperformed equivalent material loaded with NPs in terms of TOF_0 (2 orders of magnitude higher) and selectivity, which could be easily controlled through a careful choice of the type of peroxides (TBHP vs H_2O_2). On top of that, the catalyst was fully recyclable, and did not show any leaching or iron segregation, and quite uniquely it worked even with sub-stoichiometric amounts of oxidant (peroxides), Which if explored could lead to considerable advancement in the field. Analysis of various catalytic tests allowed us to propose a catalytic cycle, highlighting the central role of Fe centers in activating molecular oxygen, the final oxidant.

CRediT authorship contribution statement

Biagio Di Vizio: Writing – review & editing, Writing – original draft, Investigation, Formal analysis. **Dario Mosconi:** Writing – review & editing, Investigation, Formal analysis. **Matías Blanco:** Writing – review & editing, Writing – original draft, Formal analysis, Data curation, Conceptualization. **Panjuang Tang:** Writing – review & editing, Investigation, Formal analysis. **Luca Nodari:** Writing – review & editing, Formal analysis, Data curation. **Ondřej Tomanec:** Writing – review & editing, Formal analysis, Data curation. **Michal Otyepka:** Writing – review & editing, Formal analysis, Data curation. **Simone Pollastri:** Writing – review & editing, Formal analysis, Data curation. **Stefano Livraghi:** Writing – review & editing, Formal analysis, Data curation. **Mario Chiesa:** Writing – review & editing, Formal analysis, Data curation. **Gaetano Granozzi:** Writing – review & editing, Resources, Funding acquisition. **Stefano Agnoli:** Writing – review & editing, Formal analysis, Data curation.

Declaration of competing interest

The authors declare the following financial interests/personal relationships which may be considered as potential competing interests: Stefano Agnoli reports financial support was provided by Ministero dell'università e della ricerca della repubblica italiana. Michal Otyepka reports financial support was provided by Ministry of Education Youth and Sports of the Czech Republic. If there are other authors, they declare that they have no known competing financial interests or personal relationships that could have appeared to influence the work reported in this paper.

Data availability

Data will be made available on request.

Acknowledgements

This work was partially supported by the following projects: Italian MIUR (PRIN, Multi-e, 20179337R7, project C2 chemical complexity (CUP: C93C22009260001) and CH4.0 (CUP: D13C22003520001) under the MUR program "Dipartimenti di Eccellenza 2023–2027). M. B. gratefully acknowledges the Clarin CoFund Program (ACA17-29, 600196), funded by Gobierno del Principado de Asturias and Marie Curie Actions. P.T. acknowledge the China Scholarship Council, China for the financial support (No. 201707565021). MO acknowledges the Operational Programme Research, Development and Education – European Regional Development Fund project (CZ.02.1.01/0.0/0.0/16_019/0000754) from the Ministry of Education, Youth and Sports of the Czech Republic. Particular Materials S.R.L. (Dr. Brian Stu) is specially acknowledged for the XRD and ζ-potential measurements. Funding from the University of Padova is gratefully acknowledged. Many thanks to Professor Chiara Maurizio for the precious help in the XAS data analysis.

Appendix A. Supplementary data

Supplementary data to this article can be found online at https://doi.org/10.1016/j.cej.2024.156299.

References

[1] H. Zhang, G. Liu, L. Shi, J. Ye, Single-atom catalysts: emerging multifunctional materials in heterogeneous catalysis, Adv. Energy Mater. 8 (2018) 1701343, https://doi.org/10.1002/aenm.201701343.
[2] A. Taufiq, S. Arista, B. Sutrisno, M. Harding, B. Tribollet, M.E. Orazem, S. Joong Lee, J. Ho Yoon, Y. Pasae, S. Tangdilintin, L. Bulo, E. Lolo Allo, The contribution of heterogeneous and homogeneous catalysts towards biodiesel quality, J. Phys. Conf. Ser. 1464 (2020) 012054, https://doi.org/10.1088/1742-6596/1464/1/012054.
[3] M. Pagliaro, V. Pandarus, R. Ciriminna, F. Béland, P. DemmaCarà, Heterogeneous versus homogeneous palladium catalysts for cross-coupling reactions, ChemCatChem 4 (2012) 432–445, https://doi.org/10.1002/CCTC.201100422.
[4] D. Mosconi, M. Blanco, T. Gatti, L. Calvillo, M. Otyepka, A. Bakandritsos, E. Menna, S. Agnoli, G. Granozzi, Arene C-H insertion catalyzed by ferrocene covalently heterogenized on graphene acid, Carbon N. Y. 143 (2019) 318–328, https://doi.org/10.1016/J.CARBON.2018.11.010.
[5] S. Hübner, J.G. De Vries, V. Farina, Why does industry not use immobilized transition metal complexes as catalysts? Adv. Synth. Catal. 358 (2016) 3–25, https://doi.org/10.1002/ADSC.201500846.
[6] H. Xu, Y. Zhao, Q. Wang, G. He, H. Chen, Supports promote single-atom catalysts toward advanced electrocatalysis, Coord. Chem. Rev. 451 (2022) 214261, https://doi.org/10.1016/j.ccr.2021.214261.
[7] B.M. Trost, The atom economy–a search for synthetic efficiency, Science 254 (1991) 1471–1477, https://doi.org/10.1126/SCIENCE.1962206.
[8] F. Lü, H. Bao, Y. Mi, Y. Liu, J. Sun, X. Peng, Y. Qiu, L. Zhuo, X. Liu, J. Luo, Electrochemical CO_2 reduction: from nanoclusters to single atom catalysts, Sustain. Energy Fuels 4 (2020) 1012–1028, https://doi.org/10.1039/C9SE00776H.
[9] Y. Hu, H. Li, Z. Li, B. Li, S. Wang, Y. Yao, C. Yu, Progress in batch preparation of single-atom catalysts and application in sustainable synthesis of fine chemicals, Green Chem. 23 (2021) 8754–8794, https://doi.org/10.1039/D1GC02331D.
[10] S. De, A.S. Burange, R. Luque, Conversion of biomass-derived feedstocks into value-added chemicals over single-atom catalysts, Green Chem. 24 (2022) 2267–2286, https://doi.org/10.1039/d1gc04285h.
[11] G. Vilé, G. Di Liberto, S. Tosoni, A. Sivo, V. Ruta, M. Nachtegaal, A.H. Clark, S. Agnoli, Y. Zou, A. Savateev, M. Antonietti, G. Pacchioni, Azide-alkyne click chemistry over a heterogeneous copper-based single-atom catalyst, ACS Catal. 12 (2022) 2947–2958, https://doi.org/10.1021/acscatal.1c05610.
[12] P. Tang, S. Paganelli, F. Carraro, M. Blanco, R. Riccò, C. Marega, D. Badocco, P. Pastore, C.J. Doonan, S. Agnoli, Postsynthetic metalated MOFs as atomically dispersed catalysts for hydroformylation reactions, ACS Appl. Mater. Interfaces 12 (2020) 54798–54805, https://doi.org/10.1021/ACSAMI.0C17073/SUPPL_FILE/AM0C17073_SI_001.PDF.
[13] L.S. Panchakarla, K.S. Subrahmanyam, S.K. Saha, A. Govindaraj, H. R. Krishnamurthy, U.V. Waghmare, C.N.R. Rao, Synthesis, structure, and properties of boron- and nitrogen-doped graphene, Adv. Mater. 21 (2009) 4726–4730, https://doi.org/10.1002/ADMA.200901285.
[14] R. Li, Z. Wei, X. Gou, Nitrogen and phosphorus dual-doped graphene/carbon nanosheets as bifunctional electrocatalysts for oxygen reduction and evolution, ACS Catal. 5 (2015) 4133–4142, https://doi.org/10.1021/ACSCATAL.5B00601/SUPPL_FILE/CS5B00601_SI_001.PDF.
[15] J. Tuček, P. Błoński, Z. Sofer, P. Šimek, M. Petr, M. Pumera, M. Otyepka, R. Zbořil, Sulfur doping induces strong ferromagnetic ordering in graphene: effect of concentration and substitution mechanism, Adv. Mater. 28 (2016) 5045–5053, https://doi.org/10.1002/ADMA.201600939.

[16] D. Mosconi, D. Mazzier, S. Silvestrini, A. Privitera, C. Marega, L. Franco, A. Moretto, Synthesis and photochemical applications of processable polymers enclosing photoluminescent carbon quantum dots, ACS Nano 9 (2015) 4156–4164, https://doi.org/10.1021/ACSNANO.5B00319.

[17] H. Wang, T. Maiyalagan, X. Wang, Review on recent progress in nitrogen-doped graphene: synthesis, characterization, and its potential applications, ACS Catal. 2 (2012) 781–794, https://doi.org/10.1021/cs200652y.

[18] D. Usachov, O. Vilkov, A. Grüneis, D. Haberer, A. Fedorov, V.K. Adamchuk, A. B. Preobrajenski, P. Dudin, A. Barinov, M. Oehzelt, C. Laubschat, D.V. Vyalikh, Nitrogen-doped graphene: efficient growth, structure, and electronic properties, Nano Lett. 11 (2011) 5401–5407, https://doi.org/10.1021/NL2031037.

[19] R.J.J. Jansen, H. van Bekkum, XPS of nitrogen-containing functional groups on activated carbon, Carbon N. Y. 33 (1995) 1021–1027, https://doi.org/10.1016/0008-6223(95)00030-H.

[20] P. Lazar, R. Mach, M. Otyepka, Spectroscopic fingerprints of graphitic, pyrrolic, pyridinic, and chemisorbed nitrogen in N-doped graphene, J. Phys. Chem. C 123 (2019) 10695–10702, https://doi.org/10.1021/ACS.JPCC.9B02163.

[21] D. Wei, Y. Liu, Y. Wang, H. Zhang, L. Huang, G. Yu, Synthesis of n-doped graphene by chemical vapor deposition and its electrical properties, Nano Lett. 9 (2009) 1752–1758, https://doi.org/10.1021/NL803279T/SUPPL_FILE/NL803279T_SI_001.PDF.

[22] D. Deng, X. Pan, L. Yu, Y. Cui, Y. Jiang, J. Qi, W.X. Li, Q. Fu, X. Ma, Q. Xue, G. Sun, X. Bao, Toward N-doped graphene via solvothermal synthesis, Chem. Mater. 23 (2011) 1188–1193, https://doi.org/10.1021/cm102666r.

[23] D.D. Chronopoulos, A. Bakandritsos, M. Pykal, R. Zbořil, M. Otyepka, Chemistry, properties, and applications of fluorographene, Appl. Mater. Today 9 (2017) 60–70, https://doi.org/10.1016/j.apmt.2017.05.004.

[24] M. Dubecký, E. Otyepková, P. Lazar, F. Karlický, M. Petr, K. Čépe, P. Banáš, R. Zbořil, M. Otyepka, Reactivity of fluorographene: a facile way toward graphene derivatives, J. Phys. Chem. Lett. 6 (2015) 1430–1434, https://doi.org/10.1021/ACS.JPCLETT.5B00565.

[25] D.D. Chronopoulos, A. Bakandritsos, P. Lazar, M. Pykal, K. Čépe, R. Zbořil, M. Otyepka, High-yield alkylation and arylation of graphene via grignard reaction with fluorographene, Chem. Mater. 29 (2017) 926–930, https://doi.org/10.1021/acs.chemmater.6b05040.

[26] A. Bakandritsos, M. Pykal, P. Błoński, P. Jakubec, D.D. Chronopoulos, K. Poláková, V. Georgakilas, K. Čépe, O. Tomanec, V. Ranc, A.B. Bourlinos, R. Zbořil, M. Otyepka, Cyanographene and graphene acid: emerging derivatives enabling high-yield and selective functionalization of graphene, ACS Nano 11 (2017) 2982–2991, https://doi.org/10.1021/acsnano.6b08449.

[27] M. Blanco, S. Agnoli, G. Granozzi, Graphene acid: a versatile 2D platform for catalysis, Isr. J. Chem. 62 (2022) e202100118.

[28] R.C. Hensel, B. Di Vizio, V. Montes-García, J. Yang, G.G. Ilie, F. Sedona, M. Sambi, P. Samorì, A. Cester, S. Agnoli, S. Casalini, R.C. Hensel, B. Di Vizio, J. Yang, G.G. Ilie, F. Sedona, M. Sambi, S. Agnoli, S. Casalini, Graphene Acetic Acid-Based Hybrid Supercapacitor and Liquid-Gated Transistor, (2024). https://doi.org/10.1002/aelm.202300685.

[29] D.D. Chronopoulos, M. Medved', P. Błoński, Z. Nováček, P. Jakubec, O. Tomanec, A. Bakandritsos, V. Novotná, R. Zbořil, M. Otyepka, Alkynylation of graphene via the Sonogashira C-C cross-coupling reaction on fluorographene, Chem. Commun. 55 (2019) 1088–1091, https://doi.org/10.1039/C8CC08492K.

[30] M. Medveď, G. Zoppellaro, J. Ugolotti, D. Matochová, P. Lazar, T. Pospíšil, A. Bakandritsos, J. Tuček, R. Zbořil, M. Otyepka, Reactivity of fluorographene is triggered by point defects: Beyond the perfect 2D world, Nanoscale 10 (2018) 4696–4707, https://doi.org/10.1039/c7nr09426d.

[31] D. Zaoralová, V. Hrubý, V. Šedajová, R. Mach, V. Kupka, J. Ugolotti, A. Bakandritsos, M. Medved', M. Otyepka, Tunable synthesis of nitrogen doped graphene from fluorographene under mild conditions, ACS Sustain. Chem. Eng. 8 (2020) 4764–4772, https://doi.org/10.1021/acssuschemeng.9b07161.

[32] V. Šedajová, A. Bakandritsos, P. Błoński, M. Medveď, R. Langer, D. Zaoralová, J. Ugolotti, J. Dzíbelová, P. Jakubec, V. Kupka, M. Otyepka, Nitrogen doped graphene with diamond-like bonds achieves unprecedented energy density at high power in a symmetric sustainable supercapacitor, Energy Environ. Sci. 15 (2022) 740–748, https://doi.org/10.1039/D1EE02234B.

[33] Z. Zang, X. Zeng, M. Wang, W. Hu, C. Liu, X. Tang, Tunable photoluminescence of water-soluble AgInZnS–graphene oxide (GO) nanocomposites and their application in-vivo bioimaging, Sens. Actuators, B Chem. 252 (2017) 1179–1186, https://doi.org/10.1016/J.SNB.2017.07.144.

[34] P. Tang, B. Di Vizio, J. Yang, B. Patil, M. Cattelan, S. Agnoli, Fe, Ni-based metal-organic frameworks embedded in nanoporous nitrogen-doped graphene as a highly efficient electrocatalyst for the oxygen evolution reaction, Nanomaterials 14 (2024) 751, https://doi.org/10.3390/nano14090751.

[35] Y.-C. Lin, P.-Y. Teng, C.-H. Yeh, M. Koshino, P.-W. Chiu, K. Suenaga, Structural and chemical dynamics of pyridinic-nitrogen defects in graphene, Nano Lett. 15 (2015) 7408–7413, https://doi.org/10.1021/acs.nanolett.5b02831.

[36] C. Yang, Y. Chen, S. Zhao, R. Zhu, Z. Liu, Preparation of CoNC catalysts via heating a mixture of cobaltporphyrin and casein for ethylbenzene oxidation, RSC Adv. 6 (2016) 75707–75714, https://doi.org/10.1039/C6RA17114A.

[37] M.S. Chen, M.C. White, Combined effects on selectivity in Fe-catalyzed methylene oxidation, Science 327 (2010) 533–571, https://doi.org/10.1126/SCIENCE.1183602.

[38] V. Choudhary, J. Indurkar, V. Narkhede, R. Jha, MnO4−1 exchanged Mg–Al hydrotalcite: a stable and reusable/environmental-friendly catalyst for selective oxidation by oxygen of ethylbenzene to acetophenone and diphenylmethane to benzophenone, accessed November 21, 2021, J. Catal. 227 (2004) 257–261, https://www.academia.edu/7844151/MnO_4_1_exchanged_Mg_Al_hydrotalcite_a_stable_and_reusable_environmental_friendly_catalyst_for_selective_oxidation_by_oxygen_of_ethylbenzene_to_acetophenone_and_diphenylmethane_to_benzophenone.

[39] F. Carraro, L. Calvillo, M. Cattelan, M. Favaro, M. Righetto, S. Nappini, I. Píš, V. Celorrio, D.J. Fermín, A. Martucci, S. Agnoli, G. Granozzi, Fast one-pot synthesis of MoS_2/crumpled graphene p-n nanonjunctions for enhanced photoelectrochemical hydrogen production, ACS Appl. Mater. Interfaces 7 (2015) 25685–25692, https://doi.org/10.1021/ACSAMI.5B06668/SUPPL_FILE/AM5B06668_SI_001.PDF.

[40] P. Sekar, L. Calvillo, C. Tubaro, M. Baron, A. Pokle, F. Carraro, A. Martucci, S. Agnoli, Cobalt spinel nanocubes on N-doped graphene: a synergistic hybrid electrocatalyst for the highly selective reduction of carbon dioxide to formic acid, ACS Catal. 7 (2017) 7695–7703, https://doi.org/10.1021/ACSCATAL.7B02166/SUPPL_FILE/CS7B02166_SI_001.PDF.

[41] A. Di Cicco, G. Aquilanti, M. Minicucci, E. Principi, N. Novello, A. Cognigni, L. Olivi, Novel XAFS capabilities at ELETTRA synchrotron light source, J. Phys. Conf. Ser. 190 (2009) 012043, https://doi.org/10.1088/1742-6596/190/1/012043.

[42] B. Ravel, M. Newville, ATHENA, ARTEMIS, HEPHAESTUS: data analysis for X-ray absorption spectroscopy using IFEFFIT, J. Synchrotron Radiat. 12 (2005) 537–541, https://doi.org/10.1107/S0909049505012719.

[43] H. Feng, R. Cheng, X. Zhao, X. Duan, J. Li, A low-temperature method to produce highly reduced graphene oxide, Nat. Commun. 41 (4) (2013) 1–8, https://doi.org/10.1038/ncomms2555.

[44] B. Pan, C. Hu, L. Bai, F. Zhao, L. Dong, B. Zuo, W. Zhang, X. Wang, W. Li, Basicity-engineered graphite fluoride functionalization and beyond: an unusual reaction between ultraweak nucleophile and ultrastrong C-F bonds, Adv. Funct. Mater. 29 (2019) 1906076, https://doi.org/10.1002/adfm.201906076.

[45] Y. Li, X. Wang, W. Wang, R. Qin, W. Lai, A. Ou, Y. Liu, X. Liu, Nitrogen-doping chemical behavior of graphene materials with assistance of defluorination, J. Phys. Chem. C 123 (2019) 584–592, https://doi.org/10.1021/ACS.JPCC.8B10276/SUPPL_FILE/JP8B10276_SI_001.DOCX.

[46] M. Blanco, D. Mosconi, M. Otyepka, M. Medveď, A. Bakandritsos, S. Agnoli, G. Granozzi, Combined high degree of carboxylation and electronic conduction in graphene acid sets new limits for metal free catalysis in alcohol oxidation, Chem. Sci. 10 (2019) 9438–9445, https://doi.org/10.1039/c9sc02954k.

[47] M. Blanco, D. Mosconi, C. Tubaro, A. Biffis, D. Badocco, P. Pastore, M. Otyepka, A. Bakandritsos, Z. Liu, W. Ren, S. Agnoli, G. Granozzi, Palladium nanoparticles supported on graphene acid: a stable and eco-friendly bifunctional C-C homo- and cross-coupling catalyst, Green Chem. 21 (2019) 5238–5247, https://doi.org/10.1039/C9GC01436E.

[48] I. Szilágyi, E. Königsberger, P.M. May, Spectroscopic characterisation of weak interactions in acidic titanyl sulfate–iron(ii) sulfate solutions, Dalt. Trans. (2009) 7717, https://doi.org/10.1039/b906803a.

[49] Y. Sun, L. Silvioli, N.R. Sahraie, W. Ju, J. Li, A. Zitolo, S. Li, A. Bagger, L. Arnarson, X. Wang, T. Moeller, D. Bernsmeier, J. Rossmeisl, F. Jaouen, P. Strasser, Activity-selectivity trends in the electrochemical production of hydrogen peroxide over single-site metal-nitrogen-carbon catalysts, J. Am. Chem. Soc. 141 (2019) 12372–12381, https://doi.org/10.1021/JACS.9B05576/SUPPL_FILE/JA9B05576_SI_001.PDF.

[50] F. Luo, C.H. Choi, M.J.M. Primbs, W. Ju, S. Li, N.D. Leonard, A. Thomas, F. Jaouen, P. Strasser, Accurate evaluation of active-site density (SD) and turnover frequency (TOF) of PGM-free metal-nitrogen-doped carbon (MNC) electrocatalysts using CO Cryo adsorption, ACS Catal. 9 (2019) 4841–4852, https://doi.org/10.1021/ACSCATAL.9B00588/SUPPL_FILE/CS9B00588_SI_001.PDF.

[51] K. Artyushkova, A. Serov, S. Rojas-Carbonell, P. Atanassov, Chemistry of multitudinous active sites for oxygen reduction reaction in transition metal-nitrogen-carbon electrocatalysts, J. Phys. Chem. C 119 (2015) 25917–25928, https://doi.org/10.1021/ACS.JPCC.5B07653/SUPPL_FILE/JP5B07653_SI_001.PDF.

[52] L. Guo, Q. Huang, X.Y. Li, S. Yang, Iron nanoparticles: synthesis and applications in surface enhanced Raman scattering and electrocatalysis, Phys. Chem. Chem. Phys. 3 (2001) 1661–1665, https://doi.org/10.1039/B009951L.

[53] T. Mineva, I. Matanovic, P. Atanassov, M.T. Sougrati, L. Stievano, M. Clémancey, A. Kochem, J.M. Latour, F. Jaouen, Understanding active sites in pyrolyzed Fe-N-C catalysts for fuel cell cathodes by bridging density functional theory calculations and 57Fe Mössbauer spectroscopy, ACS Catal. 9 (2019) 9359–9371, https://doi.org/10.1021/ACSCATAL.9B02586/SUPPL_FILE/CS9B02586_SI_001.PDF.

[54] W. Liu, L. Zhang, X. Liu, X. Liu, X. Yang, S. Miao, W. Wang, A. Wang, T. Zhang, Discriminating catalytically active FeNx species of atomically dispersed Fe-N-C catalyst for selective oxidation of the C-H bond, J. Am. Chem. Soc. 139 (2017) 10790–10798, https://doi.org/10.1021/JACS.7B05130/SUPPL_FILE/JA7B05130_SI_001.PDF.

[55] G. Filoti, M.D. Kuz'min, J. Bartolomé, Mössbauer study of the hyperfine interactions and spin dynamics in <span class, Phys. Rev. B 74 (2006) 134420, https://doi.org/10.1103/PhysRevB.74.134420.

[56] R.V. Parish, Mössbauer spectroscopy and the chemical bond, Mössbauer Spectrosc. (1986) 17–69, https://doi.org/10.1017/CBO9780511524233.003.

[57] A.L. Bouwkamp-Wijnoltz, W. Visscher, J.A.R. Van Veen, E. Boellaard, A.M. Van der Kraan, S.C. Tang, On active-site heterogeneity in pyrolyzed carbon-supported iron porphyrin catalysts for the electrochemical reduction of oxygen: an in situ mössbauer study, J. Phys. Chem. B 106 (2002) 12993–13001, https://doi.org/10.1021/JP0266087.

[58] C. Ercolani, M. Gardini, G. Pennesi, G. Rossi, U. Russo, High-valent iron phthalocyanine.mu.-nitrido dimers, Inorg. Chem. 27 (2002) 422–424, https://doi.org/10.1021/IC00275A036.

[59] D. Paneva, K. Zaharieva, J. Grabis, I. Mitov, G. Vissokov, Plasma synthesis, Mössbauer spectroscopy and X-ray diffraction studies of nanosized iron oxides, Hyperfine Interact 198 (2010) 265–272, https://doi.org/10.1007/s10751-010-0192-5.
[60] X. Duan, K. O'Donnell, H. Sun, Y. Wang, S. Wang, Sulfur and nitrogen co-doped graphene for metal-free catalytic oxidation reactions, Small 11 (2015) 3036–3044, https://doi.org/10.1002/SMLL.201403715.
[61] T. Radhika, S. Sugunan, Vanadia supported on ceria: characterization and activity in liquid-phase oxidation of ethylbenzene, Catal. Commun. 8 (2007) 150–156, https://doi.org/10.1016/j.catcom.2006.05.033.
[62] K.M. Parida, S.S. Dash, Manganese containing MCM-41: synthesis, characterization and catalytic activity in the oxidation of ethylbenzene, J. Mol. Catal. A Chem. 306 (2009) 54–61, https://doi.org/10.1016/j.molcata.2009.02.022.
[63] A.R. Faraji, S. Mosazadeh, F. Ashouri, Synthesis and characterization of cobalt-supported catalysts on modified magnetic nanoparticle: green and highly efficient heterogeneous nanocatalyst for selective oxidation of ethylbenzene, cyclohexene and oximes with molecular oxygen, J. Colloid Interface Sci. 506 (2017) 10–26, https://doi.org/10.1016/J.JCIS.2017.06.100.
[64] W. Wang, N. Shang, J. Wang, X. Nie, C. Du, X. Zhou, X. Cheng, W. Gao, X. Liu, J. Huang, Y. Qiao, S. Gao, C. Wang, A stable single-atom Zn catalyst synthesized by a ligand-stabilized pyrolysis strategy for selective oxidation of C-H bonds, Green Chem. 24 (2022) 6008–6015, https://doi.org/10.1039/d2gc01831d.
[65] A.R. Faraji, F. Ashouri, Z. Hekmatian, S. Heydari, S. Mosazadeh, Organosuperbase dendron manganese complex grafted on magnetic nanoparticles; heterogeneous catalyst for green and selective oxidation of ethylbenzene, cyclohexene and oximes by molecular oxygen, Polyhedron 157 (2019) 90–106, https://doi.org/10.1016/j.poly.2018.09.030.
[66] M. Wei, A. Cai, B. Li, H. He, S. Wu, G. Zhang, F. Zhang, W. Peng, X. Fan, Y. Li, Atomically dispersed Fe–N5 sites anchored on 3D N-doped porous carbon for efficient selective oxidation of aromatic alkanes at room temperature, ACS Appl. Mater. Interfaces 14 (2022) 36007–36018, https://doi.org/10.1021/ACSAMI.2C05343.
[67] W. Zhou, W. Lu, Z. Sun, J. Qian, M. He, Q. Chen, S. Sun, Fe assisted Co-containing hydrotalcites catalyst for the efficient aerobic oxidation of ethylbenzene to acetophenone, Appl. Catal. A Gen. 624 (2021) 118322, https://doi.org/10.1016/j.apcata.2021.118322.
[68] D. Ji, N. Xi, G. Li, P. Dong, H. Li, H. Li, C. Li, P. Wang, Y. Zhao, Hydrotalcite-based CoxNiyAl1Ox mixed oxide as a highly efficient catalyst for selective ethylbenzene oxidation, Mol. Catal. 508 (2021) 111579, https://doi.org/10.1016/j.mcat.2021.111579.
[69] S.S. Lin, M.D. Gurol, Catalytic decomposition of hydrogen peroxide on iron oxide: kinetics, mechanism, and implications, Environ. Sci. Technol. 32 (1998) 1417–1423, https://doi.org/10.1021/es970648k.
[70] Y. Wang, J. Li, A. Liu, Oxygen activation by mononuclear nonheme iron dioxygenases involved in the degradation of aromatics Graphical Abstract Keywords Catalytic strategies · Crystal structure · High-valent iron species · Metabolism · Nonheme iron enzymes · Oxidative degradation · Reactive oxygen species · Ring-cleaving dioxygenase · Spectroscopy, J. Biol. Inorg. Chem. 22 (2017) 395–405, https://doi.org/10.1007/s00775-017-1436-5.
[71] Y. Sun, P. Cai, D. Yang, X. Yao, Single-site catalysis in heterogeneous electro-Fenton reaction for wastewater remediation, Chem Catal. 2 (2022) 679–692, https://doi.org/10.1016/J.CHECAT.2022.02.002.